



Article

Enhanced Photocatalytic Performance under Visible and Near-Infrared Irradiation of $\text{Cu}_{1.8}\text{Se}/\text{Cu}_3\text{Se}_2$ Composite via a Phase Junction

Li-Na Qiao, Huan-Chun Wang, Yang Shen, Yuan-Hua Lin * and Ce-Wen Nan

State Key Laboratory of New Ceramics and Fine Processing, School of Materials Science and Engineering, Tsinghua University, Beijing 100084, China; qln13@mails.tsinghua.edu.cn (L.-N.Q.); wanghc12@mails.tsinghua.edu.cn (H.-C.W.); shyang_mse@mail.tsinghua.edu.cn (Y.S.); cwnan@mail.tsinghua.edu.cn (C.-W.N.)

* Correspondence: linyh@mail.tsinghua.edu.cn; Tel.: +86-10-6277-3741

Academic Editors: Hongqi Sun and Zhaohui Wang

Received: 14 November 2016; Accepted: 10 January 2017; Published: 18 January 2017

Abstract: A novel $\text{Cu}_{1.8}\text{Se}/\text{Cu}_3\text{Se}_2$ composite photocatalyst was prepared by the simple precipitation method. This composite possesses a wide photoabsorption until the range of near-infrared light, and exhibits significantly enhanced photocatalytic activity for methyl orange degradation under visible and near-infrared light irradiation compared with bare $\text{Cu}_{1.8}\text{Se}$ and Cu_3Se_2 . The mechanism of this outstanding photocatalytic behavior can be explained by the calculated energy band positions. The efficient charge separation via a phase junction of $\text{Cu}_{1.8}\text{Se}/\text{Cu}_3\text{Se}_2$ composite would make a great contribution to its much-enhanced photocatalytic efficiency.

Keywords: $\text{Cu}_{1.8}\text{Se}/\text{Cu}_3\text{Se}_2$ composite; visible; near-infrared; photocatalysis; phase junction

1. Introduction

Semiconductor photocatalysis for the degradation of organic pollutants using solar light energy is a promising approach to solving environmental issue. Since TiO_2 was first reported on photocatalytic water splitting under ultraviolet (UV) light [1], photocatalysts have been widely studied in recent years [2–5]. Recently, photocatalysts with outstanding photocatalytic properties have been found, such as TiO_2 and ZnO in the UV spectral range [6,7], and CdS and Bi_2WO_6 in the visible range [8,9], and only few semiconductors present near-infrared (NIR) photoactivity, such as $\text{Cu}_2(\text{OH})\text{PO}_4$ and WS_2 [10,11]. Nowadays, the development of effective ways to exploit near-infrared light (which accounts for more than 50% of solar energy) and develop UV-visible-near-infrared (UV-Vis-NIR) broad light spectrum photocatalysts is an important emerging topic [12]. Forming heterogeneous structures with matched band potentials is one approach [13–15]. For example, Au-tipped $\text{PbSe}/\text{CdSe}/\text{CdS}$ core/shell/shell heterostructure nanocrystals are active NIR photocatalysts for the degradation of methylene blue (MB) [16], and $\text{Bi}_2\text{WO}_6/\text{TiO}_2$ heterojunction can harness UV, visible, and near-infrared light, and exhibits enhanced broad-spectrum photocatalytic properties to decompose methyl orange (MO) [17]. Thus, the design of a broad light spectrum photocatalyst with heterogeneous structure is of great significance.

Selenides of copper are metal chalcogenide semiconductors with different compositions (Cu_2Se , Cu_3Se_2 , CuSe , and $\text{Cu}_{1.8}\text{Se}$) and various crystallographic forms, which are usually dependent on the preparation process [18–25]. The thermal stability and band gaps of copper selenides vary with their compositions or phases [19–21]. These semiconductors with p-type conductivity and direct band gaps have wide applications in solar cells, superconductors, thermoelectric, and photoelectric transformers [26–30]. Therefore, considerable progress on the study of copper selenides has been made, and a number of methods for the synthesis of copper selenides have been explored,

such as microwave-assisted heating, sonochemical method, hydrothermal method, and vacuum evaporation [31–34].

Herein, we report on the aqueous precipitation synthesis of $\text{Cu}_{1.8}\text{Se}/\text{Cu}_3\text{Se}_2$ heterogeneous structure, bare $\text{Cu}_{1.8}\text{Se}$, and Cu_3Se_2 based on the redox reaction between alkaline selenium solution and cupric aqueous solution under atmospheric pressure. Compared with other reported methods, this method established in aqueous solution is rather simple and safe. The photocatalytic degradation of MO under visible and near-infrared (NIR) light demonstrated that $\text{Cu}_{1.8}\text{Se}/\text{Cu}_3\text{Se}_2$ composite exhibits much enhanced photocatalytic activity compared with bare $\text{Cu}_{1.8}\text{Se}$ or Cu_3Se_2 . The mechanism of enhanced photocatalytic activity for $\text{Cu}_{1.8}\text{Se}/\text{Cu}_3\text{Se}_2$ composite based on the calculated energy band positions was also proposed.

2. Results and Discussion

The composition of products was controlled by varying the addition of NaOH. As shown in Figure 1, when 0.4 g NaOH was added, the X-ray diffraction (XRD) pattern of Figure 1a matched the JCPDS reference file for tetragonal Cu_3Se_2 [PDF#65-1656]. When 4 g NaOH was included, the diffraction profile of Figure 1b shows that the composite was composed of tetragonal Cu_3Se_2 [PDF#65-1656] and cubic $\text{Cu}_{1.8}\text{Se}$ [JCPDF 06-0680]. By increasing the addition of NaOH to 8 g, the XRD pattern of Figure 1c indicates that all the peaks can be well indexed to cubic $\text{Cu}_{1.8}\text{Se}$ [JCPDF 06-0680]. No characteristic peaks of any impurities were detected in the patterns, and the high diffraction intensity reveals that all the samples had good crystallinity. In addition, the particle sizes calculated from Scherrer's equation and the BET (Brunauer-Emmett-Teller) specific surface area of different samples are shown in Table 1. There are not big difference in their particle sizes, and $\text{Cu}_{1.8}\text{Se}$ displays a larger specific surface area than $\text{Cu}_{1.8}\text{Se}/\text{Cu}_3\text{Se}_2$ composite and Cu_3Se_2 , which could lead to the exposure of more active sites for the photocatalytic experiment.

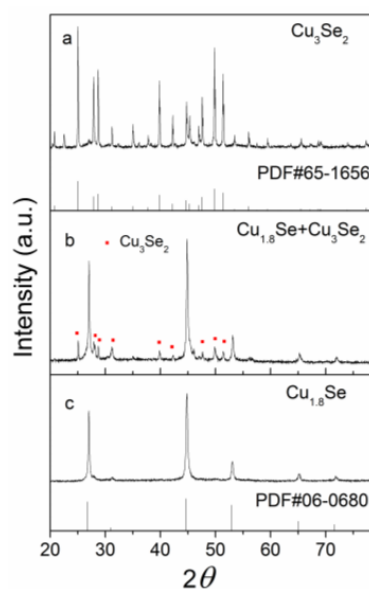


Figure 1. X-ray diffraction profiles of as-prepared copper selenides, (a) Cu_3Se_2 , (b) $\text{Cu}_{1.8}\text{Se}/\text{Cu}_3\text{Se}_2$ composite, (c) $\text{Cu}_{1.8}\text{Se}$.

Table 1. The BET (Brunauer-Emmett-Teller) specific surface area of different samples.

Samples	$\text{Cu}_{1.8}\text{Se}/\text{Cu}_3\text{Se}_2$ Composite	$\text{Cu}_{1.8}\text{Se}$	Cu_3Se_2
Size (nm)	66.3	48.6	57.8
Specific surface area (m^2/g)	5.842	8.655	6.556

The morphology and microstructure of $\text{Cu}_{1.8}\text{Se}/\text{Cu}_3\text{Se}_2$ composite are shown in the TEM (transmission electron microscopy) image of Figure 2c, with homogeneous size distribution of about 50–80 nm (in agreement with the calculated particle size in Table 1), and the bare $\text{Cu}_{1.8}\text{Se}$ (Figure 2a) and Cu_3Se_2 (Figure 2b) nanocrystals (NCs) have similar morphologies. The lattice resolved HRTEM (high resolution transmission electron microscopy) image of $\text{Cu}_{1.8}\text{Se}/\text{Cu}_3\text{Se}_2$ composite indicates the longitudinal fringe spacing of 0.331 nm and the horizontal fringe spacing of 0.354 nm (as seen in Figure 2d), which is consistent with the spacing of (111) and (101) planes of cubic $\text{Cu}_{1.8}\text{Se}$ and tetragonal Cu_3Se_2 , respectively. The high-quality image of the interface between $\text{Cu}_{1.8}\text{Se}$ and Cu_3Se_2 can be observed clearly, which could be considered as a phase junction structure [35].

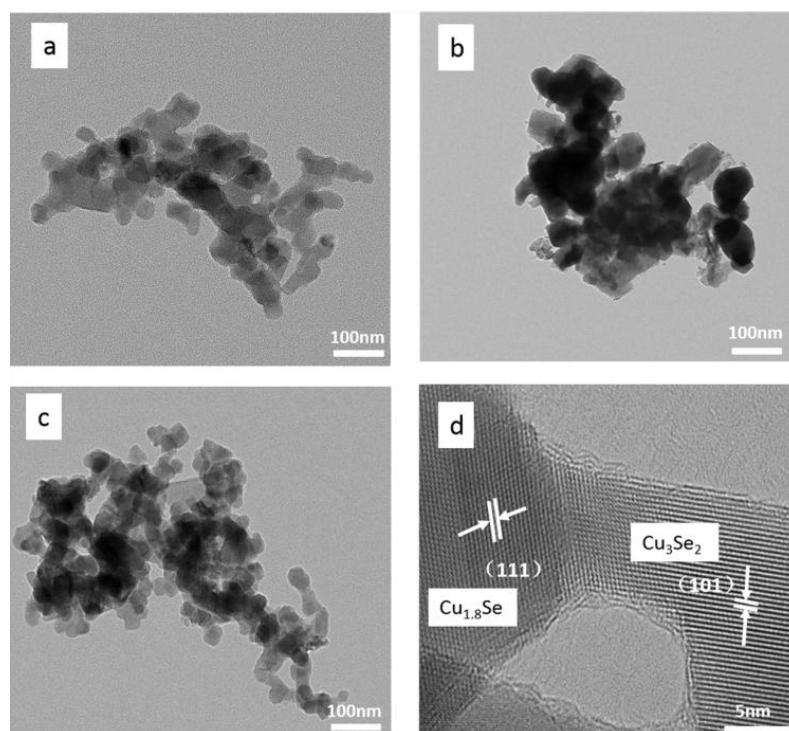


Figure 2. TEM (transmission electron microscopy) images of (a) $\text{Cu}_{1.8}\text{Se}$; (b) Cu_3Se_2 ; (c) $\text{Cu}_{1.8}\text{Se}/\text{Cu}_3\text{Se}_2$ composite; (d) HRTEM (high resolution transmission electron microscopy) of $\text{Cu}_{1.8}\text{Se}/\text{Cu}_3\text{Se}_2$ composite.

The UV-Vis diffuse reflection spectrum (DRS) of the as-prepared samples is shown in Figure 3a. It can be seen that these samples present effective optical absorption from the UV light region to the whole range of NIR light, which can be attributed to their small bandgaps. As shown in Figure 3b (converted from the DRS spectrum according to the Kubelka–Munk function [36–38]), the bandgap energies (E_g) of $\text{Cu}_{1.8}\text{Se}/\text{Cu}_3\text{Se}_2$ composite, Cu_3Se_2 , and $\text{Cu}_{1.8}\text{Se}$ were estimated to be around 1.42, 1.45, and 1.5 eV, respectively, which are similar to the reported bandgap [31,32]. It is worth noting that these bandgap values are very close, and $\text{Cu}_{1.8}\text{Se}/\text{Cu}_3\text{Se}_2$ composite has a relatively narrower band gap and stronger light absorption than that of Cu_3Se_2 and $\text{Cu}_{1.8}\text{Se}$.

The photocatalytic activities of these samples were evaluated by the photodegradation of MO under visible and NIR light irradiation. As shown in Figure 4a,b, under identical experimental conditions, the $\text{Cu}_{1.8}\text{Se}/\text{Cu}_3\text{Se}_2$ composite exhibited strongly enhanced photocatalytic activity compared to both bare $\text{Cu}_{1.8}\text{Se}$ and Cu_3Se_2 . The photodegradation rate of MO reached 80% and 75% in the presence of $\text{Cu}_{1.8}\text{Se}/\text{Cu}_3\text{Se}_2$ composite after 3 h of visible and NIR light irradiation, respectively. Thus, the $\text{Cu}_{1.8}\text{Se}/\text{Cu}_3\text{Se}_2$ composite shows relatively good visible-NIR broad light spectrum photocatalytic property, which is comparative with that of WS_2 [11] or $\text{Bi}_2\text{WO}_6/\text{TiO}_2$ [17].

By contrast, 50% and 46% of MO was degraded by bare $\text{Cu}_{1.8}\text{Se}$, whereas only 20% and 17% of MO was degraded by bare Cu_3Se_2 within the same time. Moreover, photodegradation of MO under full solar light without optical filter was performed. As shown in Figure 4c, after 2 h of full solar light irradiation, 82%, 52%, and 20% of the MO was degraded with $\text{Cu}_{1.8}\text{Se}/\text{Cu}_3\text{Se}_2$ composite, pure $\text{Cu}_{1.8}\text{Se}$, and Cu_3Se_2 as catalysts, respectively. In addition, the stabilities of these photocatalysts are shown in Figure 5. After four successive cycles, the photodegradation rate of MO under full solar light slightly decreased to 70%, 42%, and 18% within 120 min for $\text{Cu}_{1.8}\text{Se}/\text{Cu}_3\text{Se}_2$ composite, $\text{Cu}_{1.8}\text{Se}$, and Cu_3Se_2 , respectively, indicating that these materials could be re-used without appreciable loss of photocatalytic ability.

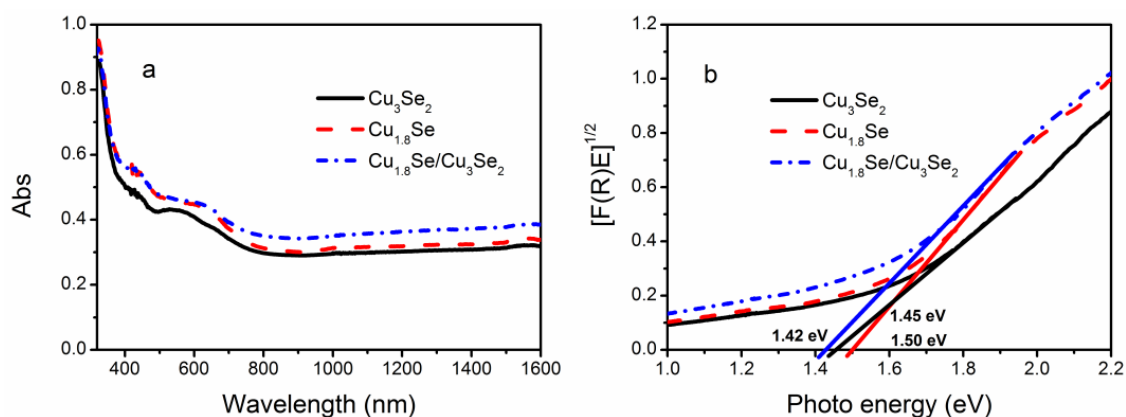


Figure 3. (a) UV-visible-near-infrared (UV-Vis-NIR) diffuse reflectance absorption (DRS) spectrum of copper selenides; (b) A plot transformed according to the Kubelka–Munk function versus energy of light.

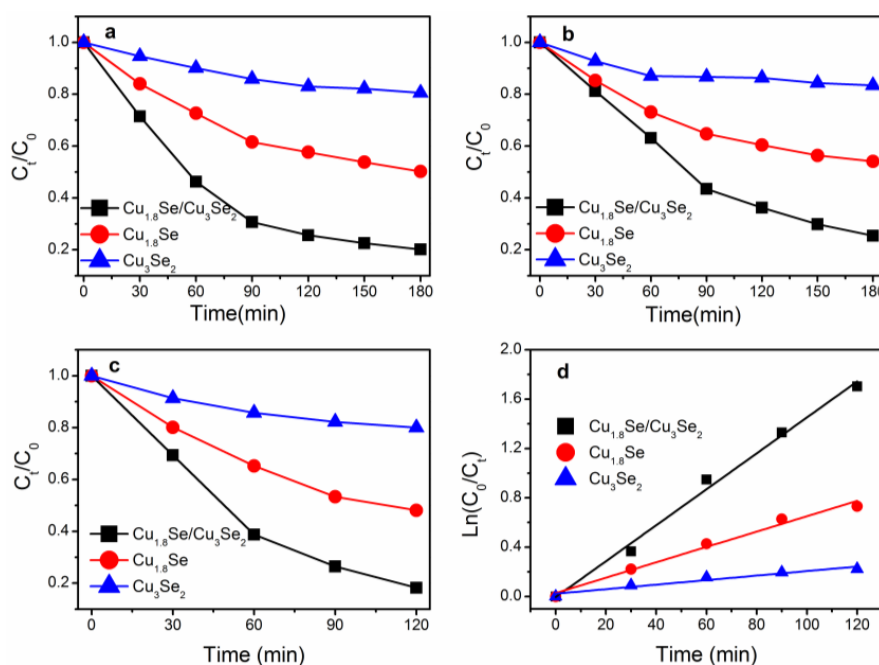


Figure 4. Photocatalytic degradation of methyl orange (MO) solution with copper selenides as catalysts under (a) visible light; (b) NIR light; (c) full solar light; (d) the degradation kinetics by means of plotting $\ln(C_0/C_t)$ versus time.

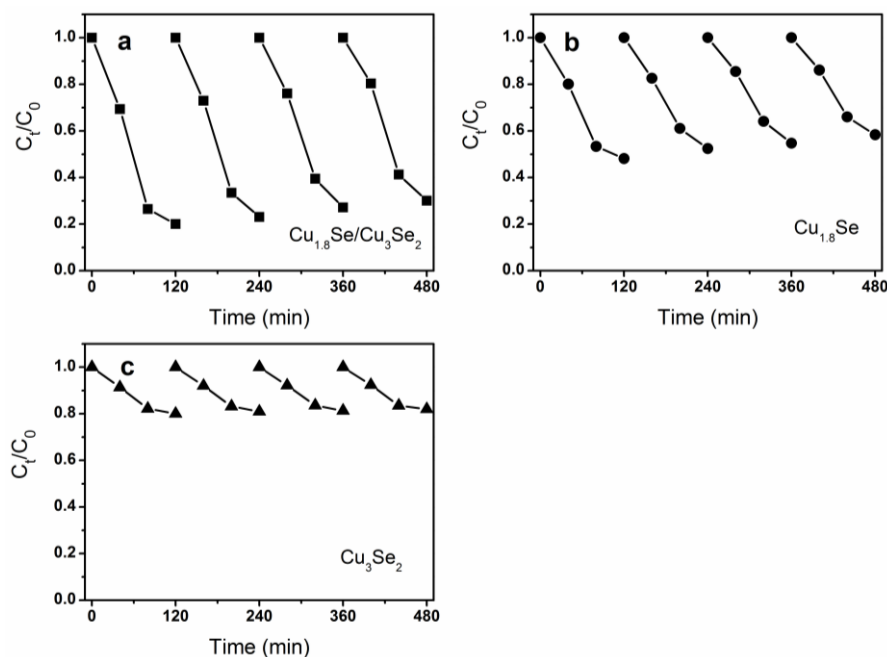


Figure 5. Cycling runs for the photocatalytic degradation of MO under full solar light in the presence of (a) $\text{Cu}_{1.8}\text{Se}/\text{Cu}_3\text{Se}_2$ composite; (b) $\text{Cu}_{1.8}\text{Se}$; (c) Cu_3Se_2 .

To further understand the reaction kinetics of MO degradation under full solar light, we applied the Langmuir–Hinshelwood model, which is well-designed for photocatalytic experiments when the concentration of the organic pollutant is in the millimolar range [39], as expressed by

$$\ln(C_0/C_t) = kt \quad (1)$$

where C_0 and C_t are the concentrations of pollutant in solution at time t_0 and t , respectively, and k is the kinetic constant, which is calculated to be 0.0145, 0.0062, and 0.0018 min^{-1} for $\text{Cu}_{1.8}\text{Se}/\text{Cu}_3\text{Se}_2$ composite, bare $\text{Cu}_{1.8}\text{Se}$, and Cu_3Se_2 , respectively (Figure 4d). Then, the apparent reaction rate constant (K) was calculated to get deeper insight into the photodegradation rate per unit surface area according to the following formula:

$$K = k/(mS) \quad (2)$$

where k is the kinetic constant from Formula (1), m is the mass of photocatalyst (0.1 g), and S is the specific surface area from Table 1. The apparent reaction rate constant (K) was calculated to be 0.0248, 0.0072, and 0.0027 min^{-1} for $\text{Cu}_{1.8}\text{Se}/\text{Cu}_3\text{Se}_2$ composite, bare $\text{Cu}_{1.8}\text{Se}$, and Cu_3Se_2 , respectively. In other words, the photocatalytic activity per unit surface area of $\text{Cu}_{1.8}\text{Se}/\text{Cu}_3\text{Se}_2$ is around 3.4 and 9.1 times higher than that of bare $\text{Cu}_{1.8}\text{Se}$ and Cu_3Se_2 .

On the other hand, X-ray photoelectron spectroscopy (XPS) analysis was carried out to investigate the chemical binding states of $\text{Cu}_{1.8}\text{Se}/\text{Cu}_3\text{Se}_2$ composite, as shown in Figure 6a,b. The Cu 2p peaks of Cu_3Se_2 and $\text{Cu}_{1.8}\text{Se}/\text{Cu}_3\text{Se}_2$ composite broaden and undergo splitting, while pronounced satellite peaks (marked as Sat.) form due to the existence of Cu^{2+} vacancy [40,41]. Two strong peaks are consistent with the literature data of Cu^+ 2p_{3/2} and 2p_{1/2} [42–44]. On the sides of Cu^+ 2p_{3/2} and 2p_{1/2} peaks, two low-intensity components appeared, which can be assigned to the Cu^{2+} oxidation state [45,46]. As illustrated in Figure 6c, the Cu 2p_{3/2} and Cu 2p_{1/2} peaks are symmetric, narrow, and devoid of satellite peaks, which is indicative of monovalent copper of Cu^+ for bare $\text{Cu}_{1.8}\text{Se}$. Therefore, the existence of Cu_3Se_2 leads to the presence of Cu^{2+} in the $\text{Cu}_{1.8}\text{Se}/\text{Cu}_3\text{Se}_2$ composite.

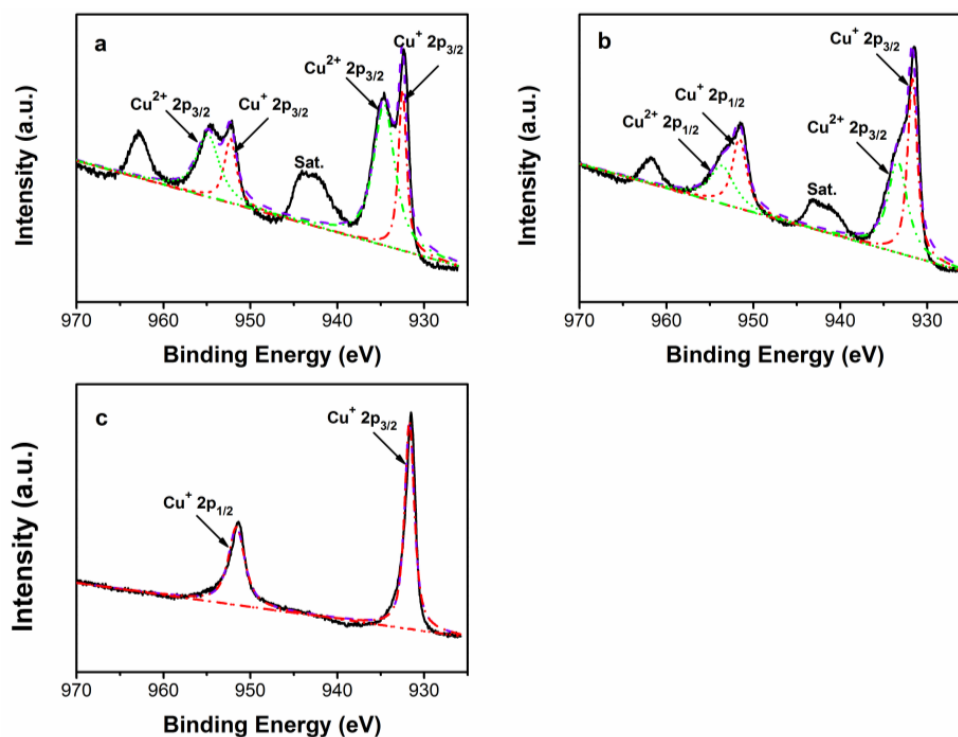


Figure 6. High-resolution X-ray photoelectron spectroscopy (XPS) scan of Cu 2p (a) Cu_3Se_2 ; (b) $\text{Cu}_{1.8}\text{Se}/\text{Cu}_3\text{Se}_2$ composite; (c) $\text{Cu}_{1.8}\text{Se}$.

In view of the mentioned XRD result (Figure 1b), $\text{Cu}_{1.8}\text{Se}$ is the main phase of $\text{Cu}_{1.8}\text{Se}/\text{Cu}_3\text{Se}_2$ composite, resulting in the smaller relative concentration ratio of Cu^{2+} to Cu^+ (1.04) than that (2.32) of bare Cu_3Se_2 . Combined with the photodegradation results (Figure 3), it could be inferred that decreasing the concentration ratio of Cu^{2+} to Cu^+ is conducive to enhancing photoactivity. It is worth noting that $\text{Cu}_{1.8}\text{Se}/\text{Cu}_3\text{Se}_2$ composite has a larger concentration ratio of Cu^{2+} to Cu^+ (1.04) than that (0) of bare $\text{Cu}_{1.8}\text{Se}$, but the best photocatalytic activity—mainly due to the existence of phase junction between $\text{Cu}_{1.8}\text{Se}$ and Cu_3Se_2 mentioned in the HRTEM image (Figure 2d).

The relative band positions of the two semiconductors were determined to account for the enhanced photocatalytic activity of the $\text{Cu}_{1.8}\text{Se}/\text{Cu}_3\text{Se}_2$ composite. The energy of conduction band (CB) bottoms (E_{CB}) were calculated empirically according to formula [47]

$$E_{\text{CB}} = X - 0.5E_{\text{g}} + E_0 \quad (3)$$

where E_{g} is the band gap of the semiconductor, E_0 is -4.5 eV for a normal hydrogen electrode, and X is the electronegativity of the semiconductor, expressed as the geometric mean of the absolute electronegativity of the constituent atoms [48]. The X values for $\text{Cu}_{1.8}\text{Se}$ and Cu_3Se_2 were calculated to be 4.94 and 5.0 eV, respectively, and the band gaps of $\text{Cu}_{1.8}\text{Se}$ and Cu_3Se_2 are 1.5 and 1.45 eV, respectively. On the basis of the equation above, the conduction band bottoms (E_{CB}) of $\text{Cu}_{1.8}\text{Se}$ and Cu_3Se_2 were calculated to be -0.31 and -0.22 eV, respectively. Correspondingly, the valence band tops (E_{VB}) of $\text{Cu}_{1.8}\text{Se}$ and Cu_3Se_2 are 1.19 and 1.23 eV, respectively. Thus, both the conduction band bottom (E_{CB}) and the valence band top (E_{VB}) of $\text{Cu}_{1.8}\text{Se}$ are higher than that of Cu_3Se_2 . The calculated band positions of $\text{Cu}_{1.8}\text{Se}/\text{Cu}_3\text{Se}_2$ composite was conducive to the separation and transportation of photogenerated carriers.

As shown in Figure 7, $\text{Cu}_{1.8}\text{Se}$ and Cu_3Se_2 are easily excited by visible or NIR light, and photoinduced electrons and holes are generated. The CB edge potentials of the two phases enable photogenerated electrons to easily transfer from $\text{Cu}_{1.8}\text{Se}$ to Cu_3Se_2 . Simultaneously, holes on

the valence band of Cu_3Se_2 can be transferred to that of $\text{Cu}_{1.8}\text{Se}$ under the band energy potential difference. In such a way, long-lived reactive photogenerated carriers can be yielded, and thus enhanced charge separation efficiency through the phase junction can be achieved.

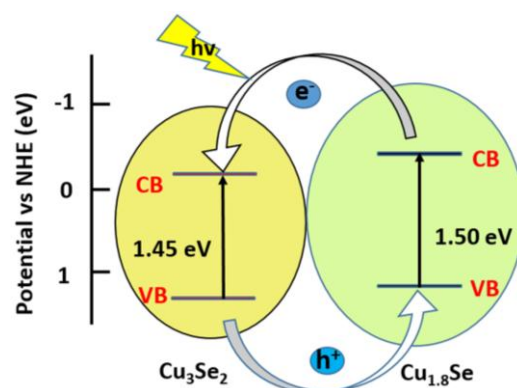


Figure 7. Diagram of energy band levels of $\text{Cu}_{1.8}\text{Se}/\text{Cu}_3\text{Se}_2$ composites vs. NHE (normal hydrogen electrode) and the possible charge separation process.

To further confirm the effect of phase junction, the photoelectrochemical (PEC) behavior of $\text{Cu}_{1.8}\text{Se}/\text{Cu}_3\text{Se}_2$ composite has been explored. As shown in Figure 8, the photocurrent responses were recorded under visible light irradiation. The electrodes ($1 \times 1 \text{ cm}^2$) demonstrated photocurrent responses around $1 \mu\text{A}/\text{cm}^2$ and $2.5 \mu\text{A}/\text{cm}^2$ for $\text{Cu}_{1.8}\text{Se}$ and $\text{Cu}_{1.8}\text{Se}/\text{Cu}_3\text{Se}_2$ composite, respectively, while the photocurrent responses of Cu_3Se_2 were not apparent. This result provides strong evidence that the formation of a phase junction between $\text{Cu}_{1.8}\text{Se}$ and Cu_3Se_2 would efficiently accelerate the separation efficiency of charge carriers. Therefore, the $\text{Cu}_{1.8}\text{Se}/\text{Cu}_3\text{Se}_2$ composite presents highly enhanced performance as compared to bare $\text{Cu}_{1.8}\text{Se}$ and Cu_3Se_2 .

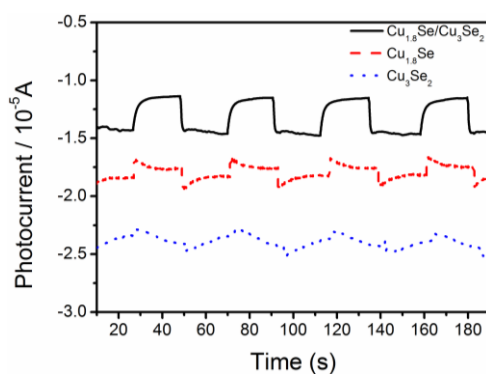


Figure 8. The photocurrent responses of copper selenides in $0.5 \text{ M Na}_2\text{SO}_4$ electrolyte under visible light.

3. Materials and Methods

3.1. Preparation

All reagents were of 99.9% purity and were used without further purification. A typical synthesis process of $\text{Cu}_{1.8}\text{Se}/\text{Cu}_3\text{Se}_2$ composite was described as follows: 4 g NaOH, 0.76 g NaBH_4 , and 0.3 g elemental Se were added to 100 mL distilled water under constant stirring. The mixture reached about $80 \text{ }^\circ\text{C}$ in a few minutes to form alkaline selenium aqueous solution. Meanwhile, 10 mL $\text{Cu}(\text{NO}_3)_2$ aqueous solution (0.5 M) was prepared, and the mixture was combined with the alkaline selenium solution through rapid stirring. Finally, 0.1 g SDS was included as surfactant to control the morphology.

After stirring for 8 h, the resulting products were separated by filtration, washed several times with distilled water and absolute alcohol, and then dried at 60 °C for 6 h. For comparison, bare Cu_3Se_2 and $\text{Cu}_{1.8}\text{Se}$ were also prepared by the hydrothermal method under the same conditions mentioned above by adding 0.4 g and 8 g NaOH, respectively.

3.2. Characterization

The phase and composition of the as-prepared samples was examined with an X-ray diffractometer (XRD, Bruker, D8 Advance, Beijing, China) using $\text{Cu K}\alpha$ radiation ($\lambda = 1.5418 \text{ \AA}$). The morphology and microstructures were characterized by transmission electron microscope (TEM, JEOL JEM-2100, Beijing, China). X-ray photoelectron spectroscopy (XPS) measurements were conducted on a Thermo XPS ESCALAB 250Xi instrument (Thermo Scientific, Shanghai, China). UV-Vis-NIR diffuser reflectance (DRS) measurements were carried out on a UV/Vis/NIR spectrometer (PerkinElmer, Lambda 950, Shanghai, China). Specific surface area measurements were conducted by Autosorb-iQ2-Mp (Quantachrome, Shanghai, China).

3.3. Photocatalytic Test

The photocatalytic activities of as-prepared samples were investigated by photodegradation of MO under visible and NIR light. A 300 W xenon lamp (CEL-HXF300, Beijing, China) with cutoff filters (420 nm, 800 nm) was used as the light source. The specific process was as follows: 0.1 g photocatalyst was added into 100 mL MO (50 mg/L). Prior to irradiation, the slurry was continuously stirred in the dark for 1 h to ensure an adsorption–desorption equilibrium between photocatalyst and MO. Ice-water bath and magnetic stirring always existed to prevent thermal effect in the photocatalytic process. At a given time interval, 3 mL suspensions were centrifuged to remove the photocatalyst. The concentration of MO was analyzed by the UV-Vis spectrophotometer by recording the variations of the absorption band maximum (465 nm).

3.4. Photoelectrochemical Testing

Photocurrent under visible light was measured with a standard three electrode system on an electrochemical workstation (CHI 660, ChenHua, Shanghai, China). Ag/AgCl and Pt plate were used as reference electrode and counter electrode, respectively, in Na_2SO_4 solution (0.5 mol/L) as electrolyte. The working electrode was made by depositing photocatalyst on the FTO (fluorine-doped tin oxide) substrate (Beijing, China).

4. Conclusions

The $\text{Cu}_{1.8}\text{Se}/\text{Cu}_3\text{Se}_2$ heterogeneous structure prepared by the simple precipitation method exhibits excellent photocatalytic activity in the degradation of MO under visible and NIR light irradiation, which is 3.4 and 9.1 times higher than that of bare $\text{Cu}_{1.8}\text{Se}$ and Cu_3Se_2 . We also present that decreasing the concentration ratio of Cu^{2+} to Cu^+ is advantageous for the enhancement of photoactivity. The mechanism of enhanced photocatalytic activity for the $\text{Cu}_{1.8}\text{Se}/\text{Cu}_3\text{Se}_2$ composite was investigated based on the calculated energy band positions. The formation of a phase junction between the two semiconductors leads to the effective separation of photogenerated electron-hole pairs, which mainly account for the strongly enhanced photoactivity.

Acknowledgments: This work was supported by the NSF of China (51221291, 51328203 and 51532003).

Author Contributions: Li-Na Qiao wrote the manuscript under the guidance of Huan-Chun Wang, Yang Shen, Yuan-Hua Lin and Ce-Wen Nan. Additionally, manuscript was corrected and edited by Huan-Chun Wang.

Conflicts of Interest: The authors declare no conflict of interest.

References

1. Fujishima, A. Electrochemical photolysis of water at a semiconductor electrode. *Nature* **1972**, *238*, 37–38. [[CrossRef](#)] [[PubMed](#)]
2. Asahi, R.; Morikawa, T.; Ohwaki, T.; Aoki, K.; Taga, Y. Visible-light photocatalysis in nitrogen-doped titanium oxides. *Science* **2001**, *293*, 269–271. [[CrossRef](#)] [[PubMed](#)]
3. Zou, Z.; Ye, J.; Sayama, K.; Arakawa, H. Direct splitting of water under visible light irradiation with an oxide semiconductor photocatalyst. *Nature* **2001**, *414*, 625–627. [[CrossRef](#)] [[PubMed](#)]
4. Gao, F.; Chen, X.; Yin, K.; Dong, S.; Ren, Z.; Yuan, F.; Yu, T.; Zou, Z.; Liu, J.M. Visible-Light Photocatalytic Properties of Weak Magnetic BiFeO₃ Nanoparticles. *Adv. Mater.* **2007**, *19*, 2889–2892. [[CrossRef](#)]
5. Abdullah, H.; Khan, M.R.; Pudukudy, M.; Yaakob, Z.; Ismail, N.A. CeO₂-TiO₂ as a visible light active catalyst for the photoreduction of CO₂ to methanol. *J. Rare Earths* **2015**, *33*, 1155–1161. [[CrossRef](#)]
6. Nakata, K.; Ochiai, T.; Murakami, T.; Fujishima, A. Photoenergy conversion with TiO₂ photocatalysis: New materials and recent applications. *Electrochim. Acta* **2012**, *84*, 103–111. [[CrossRef](#)]
7. He, Y.; Wang, Y.; Zhang, L.; Teng, B.; Fan, M. High-efficiency conversion of CO₂ to fuel over ZnO/gC₃N₄ photocatalyst. *Appl. Catal. B* **2015**, *168*, 1–8.
8. Hou, Y.-F.; Liu, S.-J.; Zhang, J.; Cheng, X.; Wang, Y. Facile hydrothermal synthesis of TiO₂-Bi₂WO₆ hollow superstructures with excellent photocatalysis and recycle properties. *Dalton Trans.* **2014**, *43*, 1025–1031. [[CrossRef](#)] [[PubMed](#)]
9. Wang, L.; Wei, H.; Fan, Y.; Gu, X.; Zhan, J. One-dimensional CdS/ α -Fe₂O₃ and CdS/Fe₃O₄ heterostructures: Epitaxial and nonepitaxial growth and photocatalytic activity. *J. Phys. Chem. C* **2009**, *113*, 14119–14125. [[CrossRef](#)]
10. Wang, G.; Huang, B.; Ma, X.; Wang, Z.; Qin, X.; Zhang, X.; Dai, Y.; Whangbo, M.H. Cu₂(OH)PO₄, a Near-Infrared-Activated Photocatalyst. *Angew. Chem. Int. Ed.* **2013**, *52*, 4810–4813. [[CrossRef](#)] [[PubMed](#)]
11. Sang, Y.; Zhao, Z.; Zhao, M.; Hao, P.; Leng, Y.; Liu, H. From UV to Near-Infrared, WS₂ Nanosheet: A Novel Photocatalyst for Full Solar Light Spectrum Photodegradation. *Adv. Mater.* **2015**, *27*, 363–369. [[CrossRef](#)] [[PubMed](#)]
12. Tong, H.; Ouyang, S.; Bi, Y.; Umezawa, N.; Oshikiri, M.; Ye, J. Nano-photocatalytic materials: Possibilities and challenges. *Adv. Mater.* **2012**, *24*, 229–251. [[CrossRef](#)] [[PubMed](#)]
13. Hou, Y.; Li, X.; Zhao, Q.; Quan, X.; Chen, G. Fabrication of Cu₂O/TiO₂ nanotube heterojunction arrays and investigation of its photoelectrochemical behavior. *Appl. Phys. Lett.* **2009**, *95*, 093108. [[CrossRef](#)]
14. Georgieva, J.; Armanyanov, S.; Valova, E.; Poullos, I.; Sotiropoulos, S. Enhanced photocatalytic activity of electrosynthesised tungsten trioxide-titanium dioxide bi-layer coatings under ultraviolet and visible light illumination. *Electrochem. Commun.* **2007**, *9*, 365–370. [[CrossRef](#)]
15. Zhang, Z.; Wang, W.; Wang, L.; Sun, S. Enhancement of Visible-Light Photocatalysis by Coupling with Narrow-Band-Gap Semiconductor: A Case Study on Bi₂S₃/Bi₂WO₆. *ACS Appl. Mater. Interfaces* **2012**, *4*, 593–597. [[CrossRef](#)] [[PubMed](#)]
16. Pak, C.; Woo, J.Y.; Lee, K.; Kim, W.D.; Yoo, Y.; Lee, D.C. Extending the Limit of Low-Energy Photocatalysis: Dye Reduction with PbSe/CdSe/CdS Core/Shell/Shell Nanocrystals of Varying Morphologies under Infrared Irradiation. *J. Phys. Chem. C* **2012**, *116*, 25407–25414. [[CrossRef](#)]
17. Tian, J.; Sang, Y.; Yu, G.; Jiang, H.; Mu, X.; Liu, H. A Bi₂WO₆-based hybrid photocatalyst with broad spectrum photocatalytic properties under UV, visible, and near-infrared irradiation. *Adv. Mater.* **2013**, *25*, 5075–5080. [[CrossRef](#)] [[PubMed](#)]
18. Stevels, A.; Jellinek, F. Phase transitions in copper chalcogenides: I. The copper-selenium system. *Recl. Trav. Chim. Pays-Bas.* **1971**, *90*, 273–283. [[CrossRef](#)]
19. Haram, S.K.; Santhanam, K.; Neumann-Spallart, M.; Levy-Clement, C. Electroless deposition on copper substrates and characterization of thin films of copper (I) selenide. *Mater. Res. Bull.* **1992**, *27*, 1185–1191. [[CrossRef](#)]
20. Shafizade, R.; Ivanova, I.; Kazinets, M. Electron diffraction study of phase transformations of the compound CuSe. *Thin Solid Films* **1978**, *55*, 211–220. [[CrossRef](#)]
21. Garcia, V.; Nair, P.; Nair, M. Copper selenide thin films by chemical bath deposition. *J. Cryst. Growth* **1999**, *203*, 113–124. [[CrossRef](#)]

22. Lakshmi, M.; Bindu, K.; Bini, S.; Vijayakumar, K.; Kartha, C.S.; Abe, T.; Kashiwaba, Y. Chemical bath deposition of different phases of copper selenide thin films by controlling bath parameters. *Thin Solid Films* **2000**, *370*, 89–95. [[CrossRef](#)]
23. Lakshmi, M.; Bindu, K.; Bini, S.; Vijayakumar, K.; Kartha, C.S.; Abe, T.; Kashiwaba, Y. Reversible $\text{Cu}_{2-x}\text{Se} \leftrightarrow \text{Cu}_3\text{Se}_2$ phase transformation in copper selenide thin films prepared by chemical bath deposition. *Thin Solid Films* **2001**, *386*, 127–132. [[CrossRef](#)]
24. Heyding, R.D.; Murray, R.M. The crystal structures of $\text{Cu}_{1.8}\text{Se}$, Cu_3Se_2 , α - and γ - CuSe , CuSe_2 , and CuSe_2II . *Can. J. Chem.* **1976**, *54*, 841–848. [[CrossRef](#)]
25. Heyding, R. The copper/selenium system. *Can. J. Chem.* **1966**, *44*, 1233–1236. [[CrossRef](#)]
26. Bhuse, V.; Hankare, P.; Garadkar, K.; Khomane, A. A simple, convenient, low temperature route to grow polycrystalline copper selenide thin films. *Mater. Chem. Phys.* **2003**, *80*, 82–88. [[CrossRef](#)]
27. Lévy-Clément, C.; Neumann-Spallart, M.; Haram, S.; Santhanam, K. Chemical bath deposition of cubic copper (I) selenide and its room temperature transformation to the orthorhombic phase. *Thin Solid Films* **1997**, *302*, 12–16. [[CrossRef](#)]
28. Chen, W.S.; Stewart, J.; Mickelsen, R. Polycrystalline thin-film $\text{Cu}_{2-x}\text{Se}/\text{CdS}$ solar cell. *Appl. Phys. Lett.* **1985**, *46*, 1095–1097. [[CrossRef](#)]
29. Dorfs, D.; Härtling, T.; Miszta, K.; Bigall, N.C.; Kim, M.R.; Genovese, A.; Falqui, A.; Povia, M.; Manna, L. Reversible Tunability of the Near-Infrared Valence Band Plasmon Resonance in Cu_{2-x}Se Nanocrystals. *J. Am. Chem. Soc.* **2011**, *133*, 11175–11180. [[CrossRef](#)] [[PubMed](#)]
30. Liu, X.; Wang, X.; Zhou, B.; Law, W.C.; Cartwright, A.N.; Swihart, M.T. Size-Controlled Synthesis of Cu_{2-x}E (E = S, Se) Nanocrystals with Strong Tunable Near-Infrared Localized Surface Plasmon Resonance and High Conductivity in Thin Films. *Adv. Funct. Mater.* **2013**, *23*, 1256–1264. [[CrossRef](#)]
31. Zhu, J.; Palchik, O.; Chen, S.; Gedanken, A. Microwave assisted preparation of CdSe , PbSe , and Cu_{2-x}Se nanoparticles. *J. Phys. Chem. B* **2000**, *104*, 7344–7347. [[CrossRef](#)]
32. Xie, Y.; Zheng, X.; Jiang, X.; Lu, J.; Zhu, L. Sonochemical Synthesis and Mechanistic Study of Copper Selenides Cu_{2-x}Se , β - CuSe , and Cu_3Se_2 . *Inorg. Chem.* **2002**, *41*, 387–392. [[CrossRef](#)] [[PubMed](#)]
33. Xu, S.; Wang, H.; Zhu, J.-J.; Chen, H.-Y. Sonochemical synthesis of copper selenides nanocrystals with different phases. *J. Cryst. Growth* **2002**, *234*, 263–266. [[CrossRef](#)]
34. Kemmler, M.; Lazell, M.; O'Brien, P.; Otway, D.; Park, J.-H.; Walsh, J. The growth of thin films of copper chalcogenide films by MOCVD and AACVD using novel single-molecule precursors. *J. Mater. Sci. Mater. Electron.* **2002**, *13*, 531–535. [[CrossRef](#)]
35. Liu, D.; Wang, J.; Zhang, M.; Liu, Y.; Zhu, Y. A superior photocatalytic performance of a novel Bi_2SiO_5 flower-like microsphere via a phase junction. *Nanoscale* **2014**, *6*, 15222–15227. [[CrossRef](#)] [[PubMed](#)]
36. Butler, M. Photoelectrolysis and physical properties of the semiconducting electrode WO_2 . *J. Appl. Phys.* **1977**, *48*, 1914–1920. [[CrossRef](#)]
37. Zhao, W.; Ma, W.; Chen, C.; Zhao, J.; Shuai, Z. Efficient degradation of toxic organic pollutants with $\text{Ni}_2\text{O}_3/\text{TiO}_{2-x}\text{B}_x$ under visible irradiation. *J. Am. Chem. Soc.* **2004**, *126*, 4782–4783. [[CrossRef](#)] [[PubMed](#)]
38. Xu, C.; Liu, Y.; Huang, B.; Li, H.; Qin, X.; Zhang, X.; Dai, Y. Preparation, characterization, and photocatalytic properties of silver carbonate. *Appl. Surf. Sci.* **2011**, *257*, 8732–8736. [[CrossRef](#)]
39. Sakkas, V.; Arabatzis, I.; Konstantinou, I.; Dimou, A.; Albanis, T.; Falaras, P. Metolachlor photocatalytic degradation using TiO_2 photocatalysts. *Appl. Catal. B* **2004**, *49*, 195–205. [[CrossRef](#)]
40. Zhang, J.; Yu, J.; Zhang, Y.; Li, Q.; Gong, J.R. Visible light photocatalytic H_2 -production activity of CuS/ZnS porous nanosheets based on photoinduced interfacial charge transfer. *Nano Lett.* **2011**, *11*, 4774–4779. [[CrossRef](#)] [[PubMed](#)]
41. Wong, L.; Chiam, S.; Huang, J.; Wang, S.; Pan, J.; Chim, W. Growth of Cu_2O on Ga-doped ZnO and their interface energy alignment for thin film solar cells. *J. Appl. Phys.* **2010**, *108*, 033702. [[CrossRef](#)]
42. Xing, C.; Zhang, Y.; Wu, Z.; Jiang, D.; Chen, M. Ion-exchange synthesis of $\text{Ag}/\text{Ag}_2\text{S}/\text{Ag}_3\text{CuS}_2$ ternary hollow microspheres with efficient visible-light photocatalytic activity. *Dalton Trans.* **2014**, *43*, 2772–2780. [[CrossRef](#)] [[PubMed](#)]
43. Yu, S.; Liu, J.; Zhu, W.; Hu, Z.-T.; Lim, T.-T.; Yan, X. Facile room-temperature synthesis of carboxylated graphene oxide-copper sulfide nanocomposite with high photodegradation and disinfection activities under solar light irradiation. *Sci. Rep.* **2015**, *5*, 16369. [[CrossRef](#)] [[PubMed](#)]

44. Riha, S.C.; Johnson, D.C.; Prieto, A.L. Cu₂Se nanoparticles with tunable electronic properties due to a controlled solid-state phase transition driven by copper oxidation and cationic conduction. *J. Am. Chem. Soc.* **2010**, *133*, 1383–1390. [[CrossRef](#)] [[PubMed](#)]
45. Ludwig, J.; An, L.; Pattengale, B.; Kong, Q.; Zhang, X.; Xi, P.; Huang, J. Ultrafast hole trapping and relaxation dynamics in p-type CuS nanodisks. *J. Phys. Chem. Lett.* **2015**, *6*, 2671–2675. [[CrossRef](#)] [[PubMed](#)]
46. Savariraj, A.D.; Viswanathan, K.K.; Prabakar, K. Influence of Cu vacancy on knit coir mat structured CuS as counter electrode for quantum dot sensitized solar cells. *ACS Appl. Mater. Interfaces* **2014**, *6*, 19702–19709. [[CrossRef](#)] [[PubMed](#)]
47. Jun, L.; Kako, T.; Jinhua, Y.; Zhigang, Z. Band structure design and photocatalytic activity of In₂O₃/N-InNbO₄ composite. *Appl. Phys. Lett.* **2009**, *95*. [[CrossRef](#)]
48. Xu, Y.; Schoonen, M.A. The absolute energy positions of conduction and valence bands of selected semiconducting minerals. *Am. Mineral.* **2000**, *85*, 543–556. [[CrossRef](#)]



© 2017 by the authors; licensee MDPI, Basel, Switzerland. This article is an open access article distributed under the terms and conditions of the Creative Commons Attribution (CC-BY) license (<http://creativecommons.org/licenses/by/4.0/>).